OPEN ACCESS

Field enhancement and extraordinary optical transmission by tapered periodic slits in gold films

New Journal of Physics
The open-access journal for physics

Field enhancement and extraordinary optical transmission by tapered periodic slits in gold films

Jonas Beermann[1,4], Thomas Søndergaard[2], Sergey M Novikov[1], Sergey I Bozhevolnyi[1], Eloïse Devaux[3] and Thomas W Ebbesen[3]

[1] Institute of Technology and Innovation (ITI), University of Southern Denmark, Niels Bohrs Allé 1, DK-5230 Odense M, Denmark
[2] Department of Physics and Nanotechnology, Aalborg University, Skjernvej 4A, DK-9220, Aalborg Øst, Denmark
[3] ISIS, CNRS et Université de Strasbourg, 8 allé G. Monge—BP 70028, 67083 Strasbourg Cedex, France
E-mail: job@iti.sdu.dk

New Journal of Physics **13** (2011) 063029 (17pp)
Received 5 April 2011
Published 17 June 2011
Online at http://www.njp.org/
doi:10.1088/1367-2630/13/6/063029

Abstract. We investigate field enhancements by one-dimensional periodic arrays of tapered slits fabricated to a high quality (nm precision) using focused ion beam milling in a 180 nm-thick gold film. Tapering of periodic slits in metal was recently shown to boost the extraordinary optical transmission (EOT) exhibited by similar, but non-tapered, plasmonic structures. Here, both simulated and experimental reflection spectra, along with high-resolution two-photon luminescence (TPL) scanning optical images and simulated electric field plots of the metal slits, are compared, revealing good correspondence between spectral dependences and field intensity enhancements (FEs) estimated via the *local* TPL. Experimentally investigated structures had a fixed taper angle $\alpha = 20.5^{\circ}$ for two different widths, $w = 80$ and 130 nm, having gaps $g = 25$ and 65 nm, respectively, both fabricated at two different periods, $\Lambda = 500$ and 700 nm. We attributed the obtained FE reaching $\sim$110 to nanofocusing and resonant interference of counter-propagating plasmons by the periodic tapered gaps. As both simulated and experimentally achieved FEs depend on taper angle, gold film thickness, period and gap of the slit arrays, the resonances can actually be tuned in the wavelength range from visible to infrared, making this configuration promising for a wide range of practical applications, e.g. within surface-enhanced spectroscopies.

[4] Author to whom any correspondence should be addressed.

Contents

1. Introduction

The phenomenon of extraordinary optical transmission (EOT) has triggered numerous investigations and findings [1] since its discovery [2], and several interesting configurations ranging from both random and periodic hole arrays [1, 2] to slit arrays [3–9] have been characterized, while new high-quality structures continue to pose more fascinating and promising applications. However, to date the majority of the investigated slit arrays have consisted of only straight slits, i.e. arrays of slits each having parallel walls through the thickness of the metal film [1, 3–9]. It is interesting to also examine in detail plasmonic slits having walls *tapered* at an angle through the metal film thickness.

Recently, one-dimensional (1D) gratings of *closed* plasmonic V-grooves were treated theoretically [10], and we experimentally investigated the field intensity enhancements (FE) ascribed to the surface plasmon (SP) nanofocusing by the closed tapered shape at the V-groove bottom [11]. In addition, we very recently investigated 2D V-groove arrays, e.g. via scanning Raman microscopy, thereby directly applying the demonstrated SP nanofocusing at the V-groove bottom, and revealing that (V-shaped) tapering is indeed among the important geometrical parameters when aiming at the fabrication of plasmonic structures with relatively large FEs suitable for surface-enhanced sensing [12].

To follow this idea, we also very recently investigated (*open*) periodic *tapered slits* in a gold film via both reflection and transmission spectra for relatively large 65 nm gaps at the bottom and slit periods of 500 and 700 nm [13]. To summarize, these investigations demonstrated that the EOT phenomenon can be influenced and even further enhanced by using tapered slits (instead of slits with parallel walls) [13]. Nevertheless, to date no direct characterization of the FEs achievable within the nm gaps of the (open) tapered slit configuration has been performed, but this could reveal additional possibilities of slits being used as substrates for surface-enhanced Raman scattering.

One well-established experimental technique for the evaluation of FE in nanostructures is two-photon photoluminescence (TPL) from metals, which was earlier described [14, 15] using spatially resolved TPL studies [16, 17] and near-field imaging [18] used in the characterization of local FEs. We have previously used TPL signals in scanning optical microscopy to facilitate direct estimations of the local FE (at a diffraction-limited resolution) achieved with various types of sample, such as individual metal nanostrips [19], periodic metal nanoparticles [20] and fractal shaped metal nanostructures [21].

In this paper, we investigate (500 and 700 nm) periodic arrays of high-quality tapered slits fabricated using focused ion beam (FIB) milling in a 180 nm-thick gold film, with the high sample quality being demonstrated via detailed scanning electron microscopy (SEM) images. Compared to our previous experimental reflection and transmission characterization of a tapered slit configuration [13], the present investigation involves much smaller gaps of only 25 nm, and the comparison with those of 65-nm-gaps. Here, we demonstrate very good agreement between experimental and simulated reflection spectra, obtained for both resonant and non-resonant excitation of the slits. In addition, we use for the first time TPL microscopy to map local FE in narrow nm-gaps at the bottom of the periodic tapered slits and obtain good correspondence between the estimated spectral FE dependence and both reflection and transmission as well as simulated spatial field distributions within the tapered slits. Finally, we show additional simulations elucidating the effect of tapered slit arrays on reflection, absorption and transmission during *regular* illumination (from the side with the widest slit opening) versus *inverse* illumination (from the side with the narrowest openings).

We expect that the new tapered slit configuration can lead to improvements in several promising applications already involving EOT, as well as in possible new applications in surface-enhanced sensing.

2. Sample geometries and reflection spectra

The experimentally investigated sample consists of 1D periodic line arrays of parallel tapered slits in a gold film, with each array covering $\sim 30 \times 30\,\mu\text{m}^2$ and separated from other arrays by at least 500 μm. The geometric parameters of the slits were a fixed taper angle $\alpha = 20.5^\circ$ for two different widths, $w = 80$ and 130 nm, having gaps on the exit side $g = 25$ and 65 nm, respectively, both fabricated at two array periods, $\Lambda = 500$ and 700 nm (figure 1(a)). The arrays were fabricated by FIB milling, and obtained SEM images show the good quality and reproducibility of each slit (figure 1(b)). Using the FIB to completely mill out the gold film across test areas, e.g., having only a few slits, and obtaining SEM images at tilted angles facilitates the characterization of the geometric tapered slit parameters (figure 1(c)).

We use reflection spectroscopy [22] to map the SP resonances of the tapered slit arrays before investigations with TPL microscopy. Our experimental setup for reflection spectroscopy has been described in detail previously for experiments with gold nanostrip antennas directly on glass substrates [19, 23]. Here, we use a similar method, but with a $\times 60$ objective (numerical aperture (NA) = 0.85) and take the reference spectra R_{gold} from the smooth gold film (instead of from the glass substrate) in order to compare directly with reflection R_{slits} from tapered slit arrays. Note that, in contrast to previous reflection spectroscopy experiments [19, 23], we do not cover the sample with index matching oil.

We support the experimental characterizations with theoretical reflection spectra simulated using the Green function surface integral equation method, recently treated in detail for *closed* V-grooves [10]. Here, we simulate reflection spectra specifically for tapered *open* slit arrays having the same geometric parameters as those of the fabricated sample (figure 2). Throughout the paper we use the refractive index 1.5 of glass for all considered wavelengths, and for gold we apply linear interpolation of the Johnson and Christy data [24] to obtain the refractive index at the wavelength of interest. In the simulation of figure 2, light is collected within an angle of $\pm 50^\circ$ and then *averaged* over a set of calculations performed for each angle of incidence (stepped by 1°) in the range 0°–50°, corresponding approximately to the NA = 0.85 objective

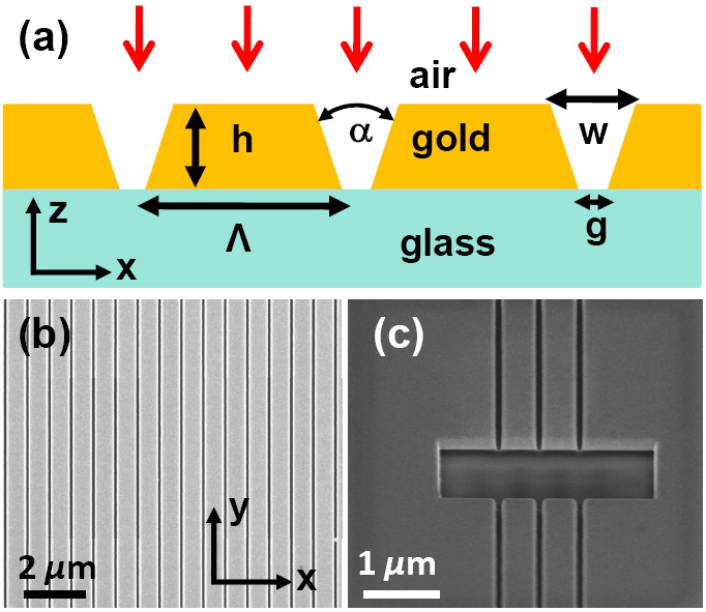

Figure 1. (a) Schematic illustration of a periodic array of tapered slits in a gold film of thickness $h = 180$ nm, supported by a glass substrate and illuminated from the top. (b) SEM image of the array with slit top width $w = 80$ nm, bottom gap $g = 25$ nm and period $\Lambda = 700$ nm; (c) zoomed SEM image of a tilted test array also with $w = 80$ nm, $g = 25$ nm but period $\Lambda = 500$ nm and cut with the FIB to demonstrate the good sample quality.

used for illumination and collection in the experiment. We also treat the theoretical results in a similar way by normalizing with respect to the reflection from a planar gold surface, thereby making simulations and experimental reflection spectra directly comparable.

We show reflection spectra for resonant p-polarized excitation and detection (figures 2(a) and (c)), i.e. with electric field in the xz-plane and perpendicular to the tapered slit, as well as for the fundamentally different non-resonant s-polarized excitation and detection (figures 2(b) and (d)), i.e. with electric field parallel to the slits [13]. First of all, it is important to note the large difference in reflection levels obtained with p- versus s-polarized configurations. In addition, for resonant p-polarized excitation and detection, the reflection spectra reveal a clear dependence on the array period (figure 2), with the shortest period ($\Lambda = 500$ nm, gaps $g = 25$ and 65 nm) exhibiting strong experimental reflection dips around the wavelength 740 nm, whereas arrays with the longer period ($\Lambda = 700$ nm, gaps $g = 25$ and 65 nm) have considerably weaker resonances approaching 700 nm for this polarization configuration (figure 2(a)). On the other hand, for the non-resonant s-polarized excitation and detection, all arrays only have a minor reflection dip fixed around 500 nm wavelength (figure 2(b)).

For each polarization configuration, there is a good correlation between the resonances appearing in simulated and experimental reflection spectra. In fact, realizing that there is a $\sim$50 nm blue shift in the experiments compared with the simulated spectra, even subtle details such as 'shoulders' or weaker dips are clearly reproduced in the simulation. Note that for s-polarized configuration the spectral termination towards unity for short wavelengths approaching 400 nm is mainly due to the limitations of the experimental setup caused by

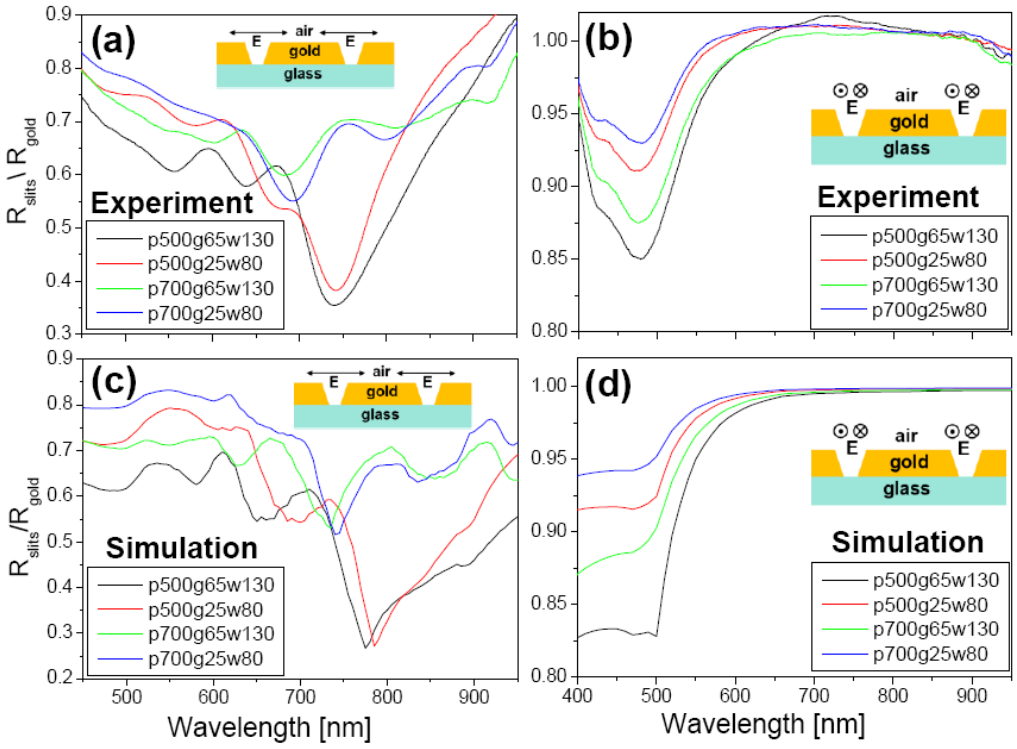

Figure 2. (a, b) Experimental and (c, d) simulated reflection spectra for p- and s-polarized excitation of structures with gaps $g = 25$ and 65 nm, taper angle $\alpha = 20.5^\circ$ and periods $\Lambda = 500$ and 700 nm. Simulated reflection spectra are equivalent to illuminating equally with all angles of incidence between -50° and $+50^\circ$, collecting reflected light within the same angular range and normalizing with reflection from a planar gold surface.

low lamp intensity and weak signals (from both the reference and the sample) in this range.

Increasing depths in the reflection spectra should be related to both increasing absorption/transmission and scattering by tapered slit arrays. Hence, the significant dip in reflectivity obtained even with a relatively high NA of 0.85, where most scattered light would actually be recollected within the large spatial angle of the objective, indicates that a major part of this dip can be ascribed to possible *changed polarization* of the scattered light, as well as to increased *absorption* or *transmission* by tapered slit arrays. For resonant p-polarized excitation and detection, the strong dips are clearly related to the array period and are relatively much less affected by slit width (figures 2(a) and (c)). Conversely, for the *non*-resonant s-polarized case increasing depth obtained in the reflection spectra is mainly governed by the larger slit width (130 nm vs 80 nm) and subsequently the shorter period Λ (500 nm vs 700 nm), in good agreement with the expected behavior, and originates from the relatively larger area (filling ratio) covered by open slits where less light is reflected (figure 2(b) and (d)). That is, according to both experiment and simulations, for the *non*-resonant case, the lowest reflection is obtained with the shortest period $\Lambda = 500$ nm and the largest width $w = 130$ nm.

3. Two-photon photoluminescence microscopy mapping local field enhancements

Our experimental setup for TPL microscopy is essentially the same as that described in detail for previous experiments [25]. It consists of a scanning optical microscope in reflection geometry built on the base of a commercial microscope and a computer-controlled 2D piezoelectric translation stage (steps down to 50 nm, accuracy ∼4 nm). The linearly polarized light beam from a mode-locked pulsed (pulse duration ∼200 fs, repetition rate ∼80 MHz) Ti-sapphire laser ($\lambda = 730$–850 nm, $\delta\lambda \sim 10$ nm, average power ∼300 mW) is used as a source of sample illumination at the fundamental harmonic (FH) frequency. After passing through an optical isolator (to avoid back-reflection), a half-wave plate, a polarizer and a wavelength selective beam splitter, the laser beam is focused on the sample surface at normal incidence with a Mitutoyo infinity-corrected ×100, NA = 0.7, objective. The illumination power is selected in the range 0.2–0.7 mW, depending on the wavelength and the obtained TPL signals. The TPL radiation generated in reflection and the reflected FH beam are collected with the same objective, separated by the wavelength-selective beam splitter, directed through appropriate filters and detected with two photomultiplier tubes, the tube for TPL photons being connected with a photon counter. The TPL detection has been improved compared with earlier investigations [25, 26], leading to very low TPL dark counts, usually ∼20 counts per second (cps).

Typical FH and TPL images ($3 \times 3\ \mu m^2$) obtained at 750 nm excitation wavelength, 100 ms integration time at each point and 50 nm steps between points for the array with 700 nm periodicity and very narrow ($w = 80$ nm) slit entrance width reveal bright lines along the slits resonantly excited at p-polarized illumination, indicated by a white arrow (figures 3(a) and (b)). Here, we do not show TPL images for the non-resonant s-polarized configuration, where we obtained relatively much weaker TPL signals, as expected from the weaker dips in the reflection spectra (figures 2(b)–(d)), and indeed a significantly stronger TPL from slits excited with p-polarized light should also be expected directly from the polarization properties of channel plasmon polaritons [29]. In order to have significant TPL signals at relatively low incident powers, we did not use polarized TPL detection. For an incident power of less than 0.7 mW, the obtained maximum TPL signal for resonant p-polarized excitation was ∼ 220 cps, which is comparable to that obtained from plasmon nanofocusing by periodic *closed* V-grooves [12].

The simultaneous recording of TPL and FH signals as a function of scan coordinates results in the matching FH and TPL images (e.g. figures 3(a) and (b)) and facilitates direct comparison of FH and TPL cross-sections (figure 3(c)). Here, the cross-sections of FH images obtained in the parallel-polarized configuration of excitation and detection replicate well (with diffraction-limited resolution) the longest 700 nm period of the slit array (figure 3(c)). The transmission as well as stronger (depolarized) scattering at the open slits causes the slits to appear dark in the FH image (figure 3(b)), compared to practically mirror-like reflection at flat areas in-between the slits. On the other hand, the TPL images exhibit the strongest signals directly from the slits and hence the resulting FH and TPL cross-sections clearly oscillate between maxima of TPL and FH, respectively (figure 3(c)). Based on the cross-sections, we estimate FH and TPL resolutions at a full-width at half-maximum of $\sim 0.7\ \mu$m and $\sim 0.5\ \mu$m, respectively.

Considering instead typical FH and TPL images from the most densely packed slit array having the widest $w = 130$ nm slit and the shortest 500 nm period (figures 4(a) and (b)), we are not able to resolve individual slits in the FH image, while it is still possible to resolve each slit

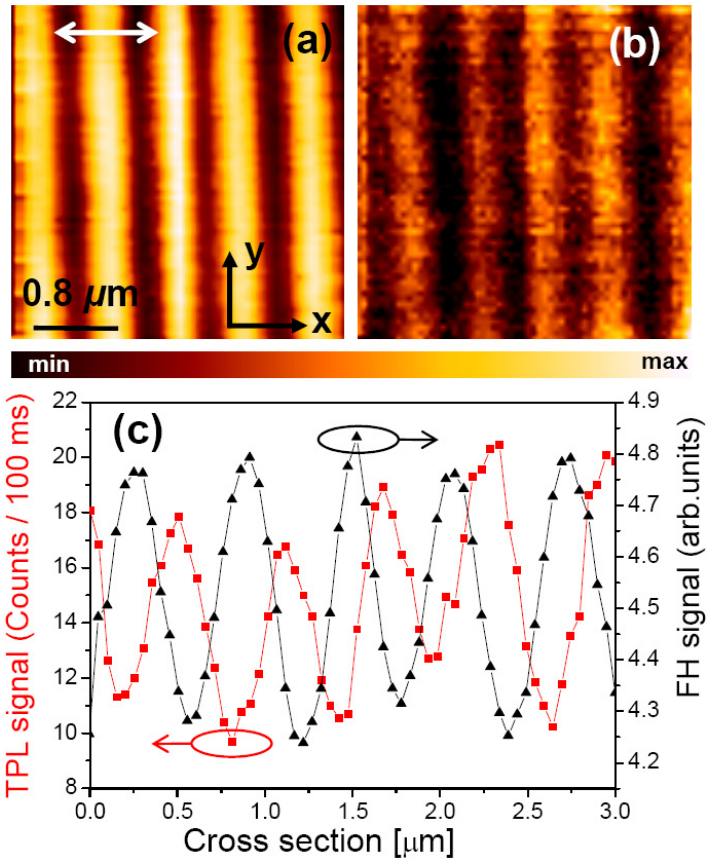

Figure 3. (a) FH and (b) TPL images of a slit array with width $w = 130$ nm, gap $g = 65$ nm, period $\Lambda = 700$ nm and depth $h = 180$ nm, obtained at $\lambda = 750$ nm for p-polarized excitation, as indicated by a white arrow on the FH image. The incident power was 0.7 mW and the maximum TPL signal 220 cps. (c) Averaged TPL (red curve, squares) and FH (black curve, triangles) intensity cross-sections taken across the slits.

in the TPL image. At the same time, cross-sections of the FH and TPL images also demonstrate these different resolution capabilities (figure 4(c)). As compared to FH images, improved TPL resolution should be expected due to the shorter wavelengths, as well as the square TPL dependence on intensity, leading generally to $\sqrt{2}$ better TPL resolution and explaining why slits are resolved in the TPL image, whereas FH images are blurred. Furthermore, the nonlinear TPL signal originates from the narrow gap at the bottom of the slits, where FE by nanofocusing is strongest, whereas the linear FH signal merely maps decreased reflection at the entire slit entrance width.

The mutual correlation between FH and TPL cross-sections obtained across slits (figure 3(c)) indicates that FH light (with polarization perpendicular to the slits) is transmitted, strongly damped or effectively scattered into other polarizations by the slits. Absorption and transmission of SPs focused towards the slit bottom dominate, as will also be demonstrated by our simulations (figure 8). For this reason, one should not expect very efficient collection of the TPL emitted at the bottom of the slits, since part of this would be reabsorbed or transmitted by

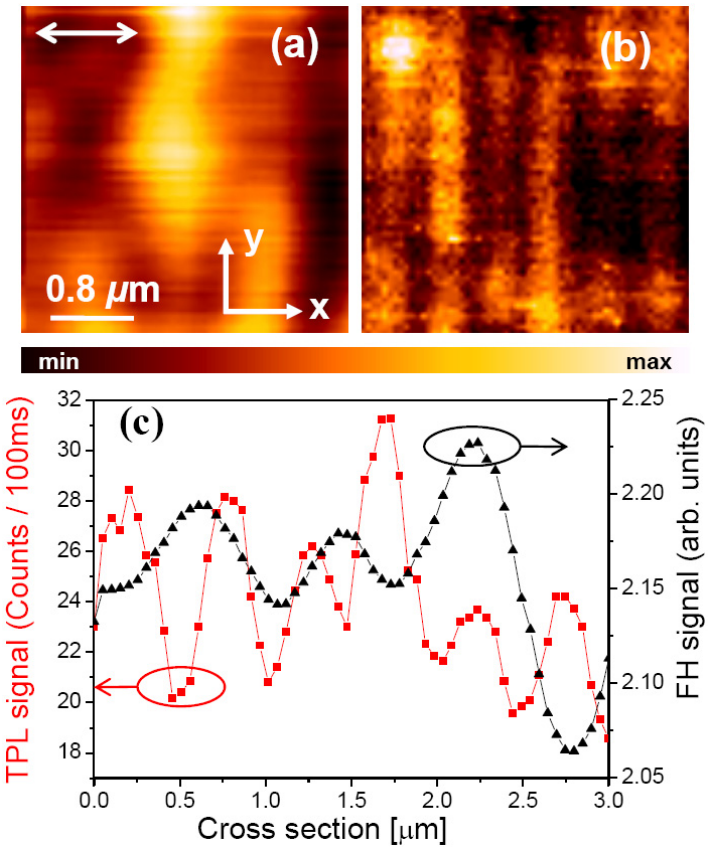

Figure 4. FH (a) and TPL (b) images of a slit array with width $w = 80$ nm, gap $g = 25$ nm, period $\Lambda = 500$ nm, and depth $h = 180$ nm, obtained at $\lambda = 730$ nm with p-polarized excitation (as indicated by the white arrow on the FH image). The incident power was 0.2 mW, and the maximum TPL signal 320 cps (c) Averaged TPL (red curve, squares) and FH (black curve, triangles) intensity cross sections taken across slits.

the slits. It should be noted here that SPs (re)-excited at the relatively short TPL wavelengths will also be damped more strongly and have considerably shorter propagation lengths of only a few micrometers.

Applications of TPL scanning optical microscopy to the characterization of local FE (of the incident FH radiation) in gold nanostructures can be considered well established [27, 28, 30]. For each slit array, we obtained TPL images of a fixed $\sim 3 \times 3\,\mu m^2$ area for six different FH excitation wavelengths in the range $\lambda = 730$–850 nm. All measurements were obtained for p-polarization, with the first five taken at wavelength steps of 15 nm and the last one shifted by 60 nm to $\lambda = 850$ nm. Taking cross-sections averaged over ten adjacent lines in these TPL images, similar to the one shown in figure 3(c), we can evaluate the dependence of typical TPL levels, e.g. those from the narrow gap of the slits, on the excitation wavelength, slit width and period.

A quantitative evaluation of FEs can be carried out by comparing TPL signals from each slit to that from a smooth gold film [27, 28, 30]. Following this approach, the FE

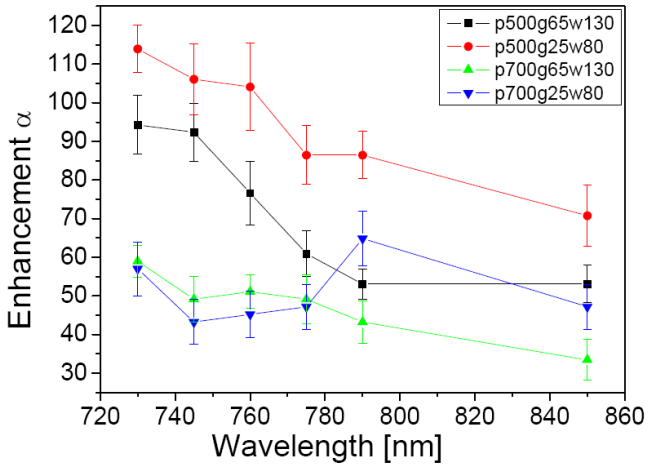

Figure 5. Experimental dependence of the intensity enhancement from the slit array on an excitation wavelength λ from 730 to 850 nm obtained for p-polarization.

factor α can be written

$$\alpha^2 = \frac{\mathrm{TPL}_{\mathrm{slit}}\langle P_{\mathrm{ref}}\rangle^2 A_{\mathrm{ref}}}{\mathrm{TPL}_{\mathrm{ref}}\langle P_{\mathrm{slit}}\rangle^2 A_{\mathrm{slit}}}, \tag{1}$$

where TPL is the obtained TPL signal, $\langle P\rangle$ is the used average incident power and A is the area producing the enhancement. Here, A_{ref} is taken as the area of the focused FH beam cross-section, i.e. $\sim\pi(0.35\,\mu\mathrm{m})^2$, whereas A_{slit} is estimated to be part of the edges closest to the slit bottom, where the expected FE is largest [13], and being illuminated along the cross-section of the focused FH beam. Based on simulations of the field magnitude distributions in slit arrays [13], we estimate the effective width actually producing TPL to be twice the projection of the lowest 1/3 of slit side walls corresponding to ~20 nm, resulting in an area $A_{\mathrm{slit}} = 0.02\,\mu\mathrm{m} \times 0.7\,\mu\mathrm{m} = 0.014\,\mu\mathrm{m}^2$, i.e. an area reduction of ~27 compared to that of the reference TPL.

At the same time, an important issue concerns the actual TPL light propagation from the slit bottom towards the detector, since this will be limited by the slit taper angle (e.g. 20.5° corresponding to NA = 0.17), which is smaller than the high NA of 0.7 used to obtain reference signals with the TPL setup. We approximate this limitation on the TPL to reach the objective by taking into account only the slit taper angle, since most of the TPL enhancement originates from the bottom of the slits where the FE is strongest. Hence, in our FE estimate we take this smaller detectable angle into account by multiplying $\mathrm{TPL}_{\mathrm{slits}}$ levels with 0.7/0.17 for a slit array having a taper angle of 20.5°.

Using calibrated TPL signals obtained from smooth gold film regions (e.g. ~2.9 kcps at $\lambda = 730$ nm and an incident FH power of 25 mW), we evaluate the FE dependence on FH excitation wavelengths from 730 to 850 nm based on TPL levels obtained in the slit arrays exposed to p-polarized light (figure 5). We estimate the largest FE factors of up to ~110 from the 500 nm periodic array having the narrow ($w = 80$ nm) slits. Indeed, the slit arrays with the shortest 500 nm period, having a significant dip in reflection spectra around 740 nm, should

be expected to exhibit the largest FE for excitation wavelengths in this range. Likewise, the significantly lower FE for arrays with a larger (700 nm) period is also in good agreement with the lower and decreasing dips in reflection spectra at wavelengths above 730 nm (figures 2(a) and (c)). All in all, within the wavelength interval 730–850 nm accessible with our excitation laser and detection range of the experimental setup, we obtain qualitatively good agreement of the estimated FEs (figure 5) with the shape expected from both experimental and simulated reflection spectra (figures 2(a) and (c)). Since the main TPL originates from the resonant p-polarized excitation of the slits (cf also spectra, figures 2(b) and (d)), we only estimated the FE levels achieved in that configuration.

4. Simulations for air-suspended one-dimensional slit arrays

The theoretical simulations presented throughout this paper have all been obtained with the Green's function surface integral equation method for periodic structures [31, 32], where the version of the method that we have used is identical to that described in more detail in our previous work [10], with the exception that in the case where we consider a perforated gold film placed on a glass substrate (figures 2(c) and (d)) we use a different Green's function. Very briefly, the method is based on an identity that allows us to calculate the magnetic field at any position outside scatterers as the sum of an incident field and an integral over the surfaces of scatterers, where the integrand involves a reference-medium Green's function, the magnetic field at the surfaces and the surface normal-derivative of the magnetic field. For positions inside scatterers, a similar relation exists, but with no incident field and with the Green's function modified for the material of the scatterers. Self-consistent equations for the magnetic field and its normal derivative at the surface of scatterers are obtained by letting the observation point approach the surfaces from both sides and by applying the electromagnetic boundary conditions. The resulting equations are discretized and solved on a computer, whereby we obtain the surface magnetic field and its normal derivative, and the starting equations can then be used to directly calculate the field at any other position of interest. For numerical reasons all corners in the considered geometries have been rounded with a 2 nm radius of curvature.

4.1. Tunability of resonances

For the above characterization the designed structure had intended resonances and spectral details in the detection range of our TPL microscopy setup. Here, we demonstrate the wide possibilities of tuning the resonances by proper adjustments of the slit taper angle, period, gold film thickness (slit depth) and gap width. Note that the spectra to be presented in figures 6–9 are all obtained with plane wave illumination and therefore cannot be directly compared to the simulated (and measured) reflection spectra in figure 2, where we average over illumination angles within $\pm 50^\circ$ (NA of the objective).

We begin by visualizing the calculated electric field magnitude around periodic tapered slits in a gold film of fixed thickness $h = 200$ nm, suspended in air with tapered slits having fixed gap $g = 10$ nm, period $\Lambda = 500$ nm and taper angle $\alpha = 20^\circ$, and excited with p-polarized light at the resonance wavelength $\lambda = 825$ nm (figure 6(a)). The electric field is indeed increased significantly by the periodic openings on the front side and focused towards the gap on the exit side via SPs in the tapered slits, where the *maximum* relative field magnitude exceeds $\sim$35 (figure 6(a)). To investigate the influence of varying the slit taper angle α as well as the period

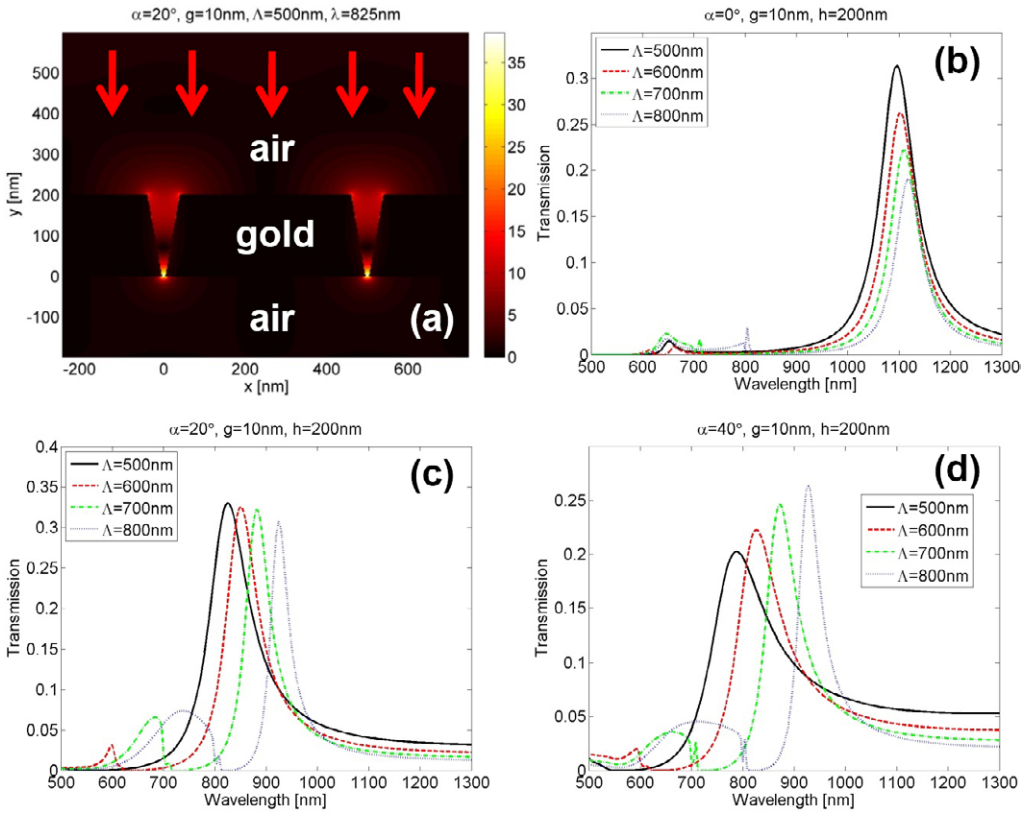

Figure 6. (a) Simulated magnitude of the electric field around a gold film of fixed thickness $h = 200$ nm, suspended in air with tapered slits having fixed gap $g = 10$ nm, period $\Lambda = 500$ nm and taper angle $\alpha = 20^\circ$, and visualized at the resonance wavelength $\lambda = 825$ nm; (b–d) transmission spectra simulated for tapered slit arrays with period $\Lambda = 500$, 600, 700 or 800 nm and having taper angle (b) $\alpha = 0^\circ$, (c) 20° and (d) 40°, all being illuminated with normally incident p-polarized light.

Λ, we also present a series of simulated transmission spectra for p-polarized light incident on 12 different arrays with period $\Lambda = 500$, 600, 700 or 800 nm and taper angle $\alpha = 0^\circ$, 20° or 40° in a gold film of fixed thickness $h = 200$ nm, with fixed slit gaps $g = 10$ nm at the exit side (figures 6(b)–(d)). It is observed that an isolated increase of the period Λ leads to a red-shifted resonance position (cf any fixed taper angle of figures 6(b)–(d)), whereas the increasing of the taper angle α leads to a blue-shifted resonance position (figures 6(b)–(d)). At the same time these transmission spectra demonstrate a much improved tunability accessible by just varying the period of the slit arrays when the taper angle is relatively large, e.g. $\alpha = 40^\circ$ as in figure 6(d). That is, the redshift in resonance position when selecting array periods Λ from 500 to 800 nm is only $\sim$30 nm for straight slits (having taper angle $\alpha = 0$), compared with the much larger redshift of $\sim$150 nm available for slit arrays with taper angle $\alpha = 40^\circ$.

Note that, in the above discussion, we still did not apply the additional tunability available by adjusting also the film thickness and gap size. Here, an alternative way of demonstrating the large tunability can be to show the possibility of actually keeping a certain resonance position fixed by simultaneous proper adjustment of several parameters, whose separate adjustment

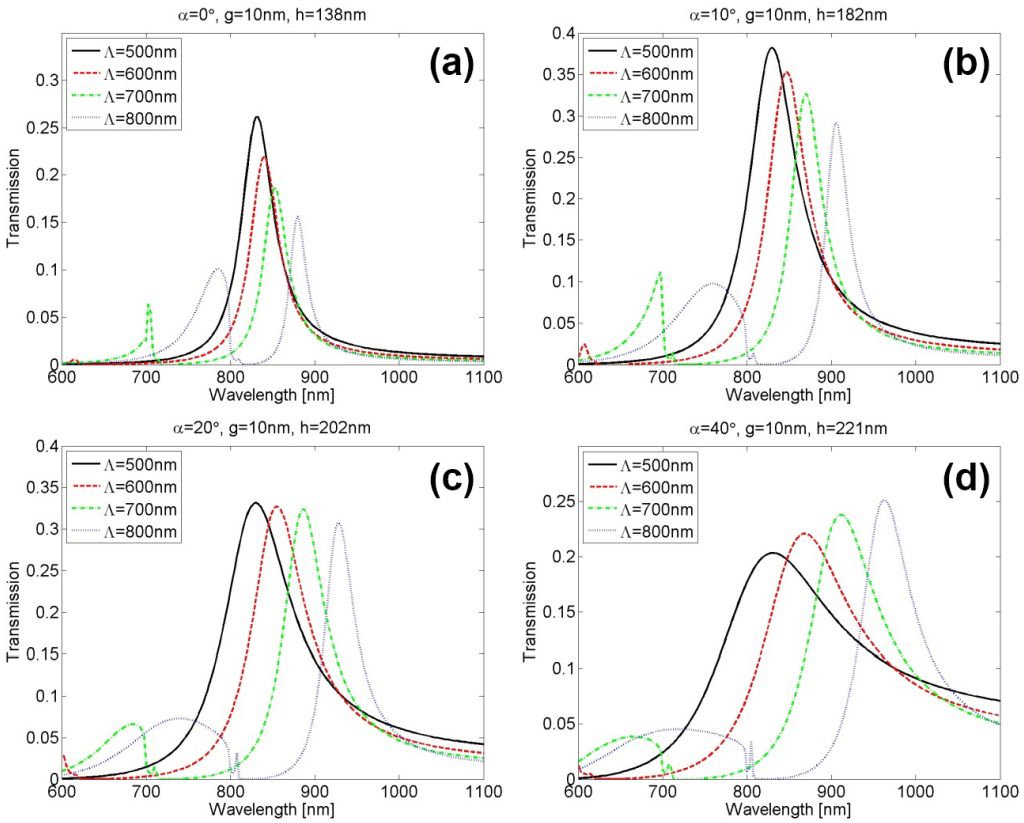

Figure 7. Transmission spectra simulated for tapered slit arrays of period $\Lambda =$ 500, 600, 700 or 800 nm, fixed gap $g = 10$ nm and taper angle (a) $\alpha = 0^\circ$, (b) 10°, (c) 20° and (d) 40°, all being illuminated with normally incident p-polarized light. For each taper angle (a–d) the gold film thickness h is adjusted so as to maintain the resonance position for the 500 nm periodic array at the wavelength $\lambda = 830$ nm.

would each lead to significant shifts in resonance. In figure 7, we use this approach to keep a resonance fixed around 830 nm, while still modifying the sample geometry by simultaneous adjustments of taper angle $\alpha = 0^\circ$–40° and film thickness (height $h = 138$–221 nm). In this connection, it should be noted that the resonance position can only be kept fixed for one array period at a time, since each period responds proportionally to adjustments in film thickness and slit taper angle. Again, the transmission spectra also demonstrate the widest tunability by array period for the largest slit taper angle of $\alpha = 40^\circ$ (figure 7(d)). The influence of gap size will be demonstrated in figure 8.

4.2. Regular versus inverse orientation of illumination

In all of the above results, we selected the illumination direction from the wide side of the slit towards the narrow gap at the slit bottom (cf e.g. figure 6(a)). However, according to the reciprocity theorem, transmission through the slit array should actually be independent of the direction of illumination, i.e. of whether the illumination is *regular*, from the front, or *inverse*, from the rear of the slit array. This means that in a sense both nanofocusing of light and the reverse situation of nanodefocusing of light, corresponding to the tapered slit opening becoming

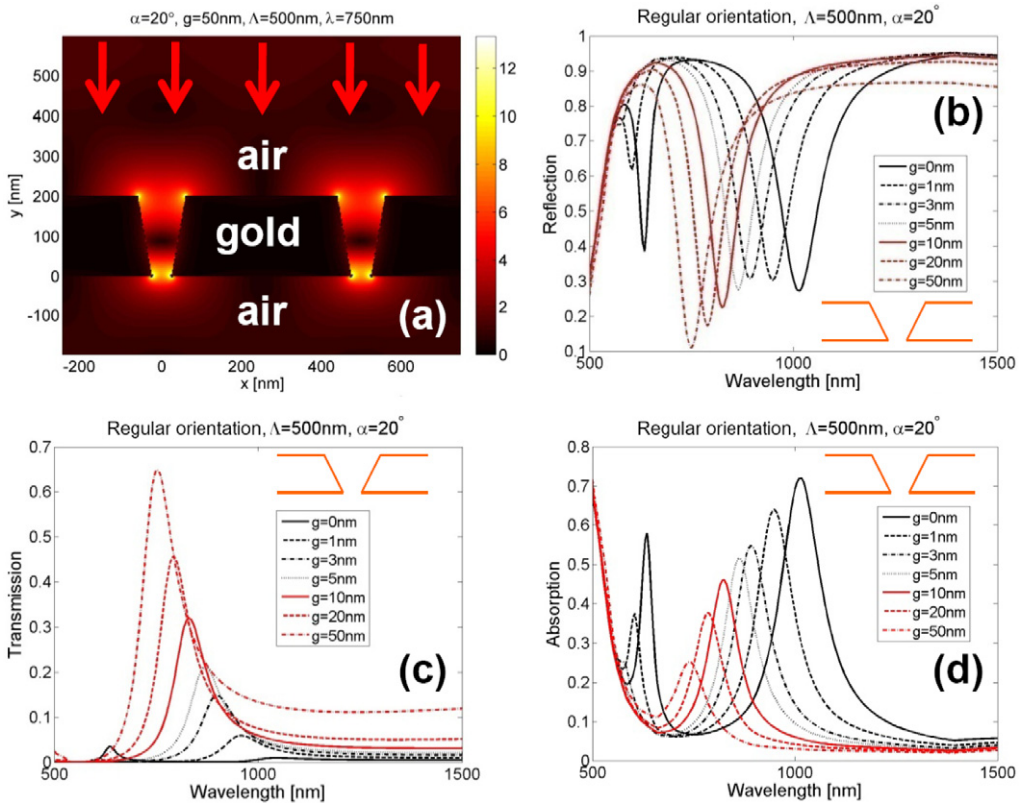

Figure 8. (a) Simulated electric field magnitude around a gold film of fixed thickness $h = 200\,\text{nm}$, period $\Lambda = 500\,\text{nm}$ and taper angle $\alpha = 20^\circ$ being suspended in air and visualized for the resonance wavelength $\lambda = 750\,\text{nm}$ and gap $g = 50\,\text{nm}$, along with (b) reflection, (c) transmission and (d) absorption spectra for the same array simulated with various gaps $g = 0$, 1, 3, 5, 10, 20 and 50 nm, and all illuminated with normally incident p-polarized light in *regular orientation*, as indicated by red arrows in (a).

smaller or larger in the direction of transmission through the structure, have exactly the same effect on the transmission [13]. Meanwhile, the reflection and absorption will in general be different in the two situations, and consequently it can be interesting to follow their behavior during illumination with both regular and inverse sample orientation.

As an example, we first visualize the simulated electric field magnitude around a 200-nm-thick air-suspended gold film with slit taper angle $\alpha = 20^\circ$, gap $g = 50\,\text{nm}$ and period $\Lambda = 500\,\text{nm}$ during plane wave illumination with p-polarized light at the resonance wavelength of $\lambda = 750\,\text{nm}$ in *regular orientation*, as indicated by red arrows (figure 8(a)). This configuration is similar to that investigated via TPL microscopy in figure 4, except for having slightly smaller gaps $g = 25\,\text{nm}$ and the gold film being deposited on a glass substrate. From the visualized electric field magnitude one can imagine how illumination at the regular orientation of this array leads to nanofocusing and fields enhanced by a factor of ~13 towards the narrow gap side in the tapered slit (figure 8(a)). By squaring this enhancement factor for the field magnitude we obtain an FE (field intensity enhancement) of ~169, compared with the FE of ~110 estimated via TPL microscopy (figure 5).

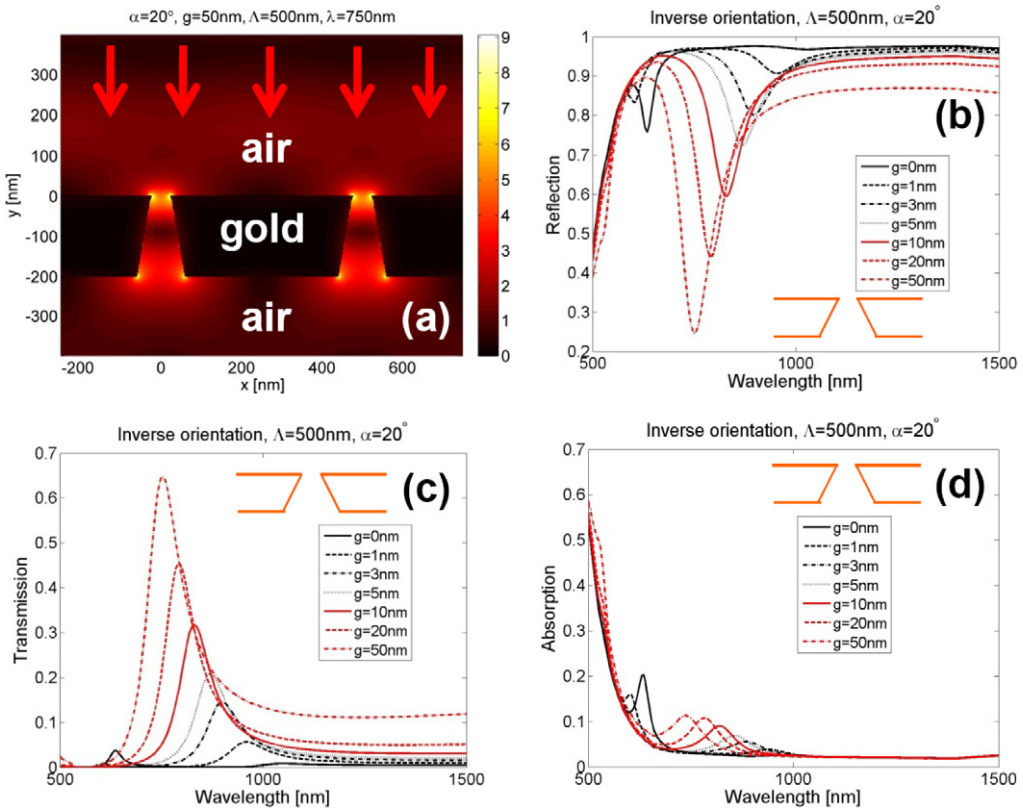

Figure 9. The same as in figure 8, but now illuminated in *inverse orientation*, i.e. light is normally incident at the narrow end of the slits (and still at p-polarization).

Furthermore, simulated reflection, transmission and absorption spectra for the above array geometry ($h = 200$ nm, $\alpha = 20^\circ$ and $\Lambda = 500$ nm) with various gaps $g = 0$, 1, 3, 5, 10, 20 and 50 nm, all being illuminated with p-polarized light in the *regular orientation*, reveal strong dips in the reflection (up to 90% decrease in reflection at the resonance wavelength for the largest gap), as well as relatively high absorption levels through the narrowing slits (figures 8(b)–(d)). In contrast, for *inverse orientation* of the slit array the field magnitude does not show the same concentration of light and the absorption is much less (figure 9).

For the regular orientation, the much larger absorption experienced when 'squeezing' light through the narrowing bottom of the slit is compensated for by lower reflection at the wide slit entrance. Likewise, for the inverse orientation the absorption in expanding slit openings is relatively lower, whereas the reflection is instead rather high due to the encountered larger area covered by flat metal and only very narrow slit openings in the metal (gaps $g = 0$–50 nm). Anyway, as expected from the reciprocity theorem, transmission is actually the same for regular and inverse illumination (figures 8(c) and 9(c)). These additional simulations elucidate the effect on reflection, absorption and transmission during regular versus inverse illumination and one could in fact also literally state: 'EOT is enhanced by nano-de-focusing'. On the other hand, the local FE is related in particular to the absorption and therefore the FE differs for the two excitation directions. Hence, *if* one could perform TPL on gaps from the rear, one would obtain different TPL signals. However, one should remember that the simulated results (figures 6–9)

were all obtained for symmetric air–gold–air configurations and for the current experimental sample, fabricated on a relatively thick glass substrate, we did not have the possibility of performing accurate TPL investigations in the inverse illumination orientation.

5. Conclusion

In conclusion, we have investigated FEs by 1D periodic arrays of tapered slits fabricated with high quality (nm precision) using FIB milling in a 180 nm-thick gold film. Tapering of the periodic slits in metal was recently shown to boost the EOT exhibited by similar, but non-tapered, plasmonic structures.

We compared both simulated and experimental reflection spectra, along with high-resolution TPL scanning optical images and simulated electric field plots of the metal slits, revealing good correspondence between the spectral dependences and *local* TPL. The experimentally investigated structures had a fixed taper angle $\alpha = 20.5^{\circ}$ for two different widths, $w = 80$ and 130 nm, having gaps $g = 25$ and 65 nm, respectively, fabricated at two different periods, $\Lambda = 500$ and 700 nm. We attributed the obtained FEs reaching $\sim$110 to nano-focusing and resonant interference of counter-propagating plasmons by the periodic tapered gaps.

Since both simulated and experimentally achieved FEs depend on taper angle, gold film thickness and period and gap of the slit arrays, the resonances can actually be tuned in the wavelength range from visible to infrared, making this new tapered slit configuration promising for improving a wide range of practical applications already involving EOT, as well as for possible new advances, e.g. within surface-enhanced spectroscopies and sensing [33–35].

Acknowledgments

The authors gratefully acknowledge financial support from the Danish Council for Independent Research (FTP contract no. 09-072949), the Lundbeck Foundation (contract no. R49-A5871) and the European Research Council (Advanced Study grant no. 227577).

References

[1] García-Vidal F J, Martin-Moreno L, Ebbesen T W and Kuipers L 2010 Light passing through subwavelength apertures *Rev. Mod. Phys.* **82** 729

[2] Ebbesen T W, Lezec H J, Ghaemi H F, Thio T and Wolff P A 1998 Extraordinary optical transmission through sub-wavelength hole arrays *Nature* **391** 667

[3] Porto J A, García-Vidal F J and Pendry J B 1999 Transmission resonances on metallic gratings with very narrow slits *Phys. Rev. Lett.* **83** 2845

[4] García-Vidal F J and Martn-Moreno L 2002 Transmission and focusing of light in one-dimensional periodically nanostructured metals *Phys. Rev.* B **66** 155412

[5] Schröter U and Heitmann D 1998 Surface-plasmon-enhanced transmission through metallic gratings *Phys. Rev.* B **58** 15419

[6] Pacifici D, Lezec H J, Atwater H and Weiner J 2008 Quantitative determination of optical transmission through subwavelength slit arrays in Ag films: role of surface wave interference and local coupling between adjacent slits *Phys. Rev.* B **77** 115411

[7] Barbara A, Quémerais P, Bustarrat E and Lopez-Rioz T 2002 Optical transmission through subwavelength metallic gratings *Phys. Rev.* B **66** 161403
[8] Sun Z, Jung Y S and Kim H K 2003 Role of surface plasmons in the optical interaction in metallic gratings with narrow slits *Appl. Phys. Lett.* **83** 3021
[9] Billaudeau C, Collin S, Pardo F, Bardou N and Pelouard J-L 2009 Tailoring radiative and non-radiative losses of thin nanostructured plasmonic waveguides *Opt. Express* **17** 3490
[10] Søndergaard T and Bozhevolnyi S I 2009 Surface-plasmon polariton resonances in triangular-groove metal gratings *Phys. Rev.* B **80** 195407
[11] Søndergaard T, Bozhevolnyi S I, Beermann J, Novikov S M, Devaux E and Ebbesen T W 2010 Resonant plasmon nanofocusing by closed tapered gaps *Nano Lett.* **10** 291–5
[12] Beermann J, Novikov S M, Søndergaard T, Rafaelsen J, Pedersen K and Bozhevolnyi S I 2011 Localized field enhancements in two-dimensional V-groove metal arrays *J. Opt. Soc. Am.* B **28** 372–8
[13] Søndergaard T, Bozhevolnyi S I, Novikov S M, Beermann J, Devaux E and Ebbesen T W 2010 Extraordinary optical transmission enhanced by nanofocusing *Nano Lett.* **10** 3123–8
[14] Mooradian A 1969 Photoluminescence of metals *Phys. Rev. Lett.* **22** 185–7
[15] Boyd G T, Yu Z H and Shen Y R 1986 Continuum generation from single gold nanostructures through near-field mediated intraband transitions *Phys. Rev.* B **33** 7923–36
[16] Beversluis M R, Bouhelier A and Novotny L 2003 Continuum generation from single gold nanostructures through near-field mediated intraband transitions *Phys. Rev.* B **68** 115433
[17] Ghenuche P, Cherukulappurath S, Taminiau T H, van Hulst N F and Quidant R 2008 Spectroscopic mode mapping of resonant plasmon nanoantennas *Phys. Rev. Lett.* **101** 116805
[18] Bouhelier A, Beversluis M R and Novotny L 2003 Characterization of nanoplasmonic structures by locally excited photoluminescence *Appl. Phys. Lett.* **83** 5041–3
[19] Beermann J, Novikov S M, Søndergaard T, Boltasseva A E and Bozhevolnyi S I 2008 Two-photon mapping of localized field enhancements in thin nanostrip antennas *Opt. Express* **16** 17302–9
[20] Beermann J and Bozhevolnyi S I 2005 Two-photon luminescence microscopy of field enhancement at gold nanoparticles *Phys. Status Solidi* c **2** 3983–7
[21] Beermann J, Evlyukhin A, Boltasseva A and Bozhevolnyi S I 2008 Nonlinear microscopy of localized field enhancements in fractal shaped periodic metal nanostructures *J. Opt. Soc. Am.* B **25** 1585–92
[22] Hohenau A, Krenn J R, Beermann J, Bozhevolnyi S I, Rodrigo S G, Martin-Moreno L and Garcia-Vidal F 2006 Spectroscopy and nonlinear microscopy of Au nanoparticle arrays: experiment and theory *Phys. Rev.* B **73** 155404
[23] Søndergaard T, Beermann J, Boltasseva A E and Bozhevolnyi S I 2008 Slow-plasmon resonant-nanostrip antennas: analysis and demonstration *Phys. Rev.* B **77** 115420
[24] Johnson P B and Christy R W 1972 Optical constants of the noble metals *Phys. Rev.* B **6** 4370
[25] Beermann J and Bozhevolnyi S I 2004 Microscopy of localized second-harmonic enhancement in random metal nanostructures *Phys. Rev.* B **69** 155429
[26] Beermann J, Bozhevolnyi S I, Pedersen K and Fage-Pedersen J 2003 High-resolution second-harmonic microscopy of poled silica waveguides *Opt. Commun.* **221** 295–300
[27] Schuck P J, Fromm D P, Sundaramurthy A, Kino G S and Moerner W E 2005 Improving the mismatch between light and nanoscale objects with gold bowtie nanoantennas *Phys. Rev. Lett.* **94** 017402
[28] Mühlschlegel P, Eisler H-J, Martin O J F, Hecht B and Pohl D W 2005 Resonant optical antennas *Science* **308** 1607–9
[29] Bozhevolnyi S I, Volkov V S, Devaux E, Laluet J-Y and Ebbesen T W 2006 Channel plasmon subwavelength waveguide components including interferometers and ring resonators *Nature* **440** 508–11
[30] Hohenau A, Krenn J R, Garcia-Vidal F J, Rodrigo S G, Martin-Moreno L, Beermann J and Bozhevolnyi S I 2007 Spectroscopy and nonlinear microscopy of gold nanoparticle arrays on gold films *Phys. Rev.* B **75** 085104
[31] Kobidze G, Shanker B and Nyquist D P 2005 Efficient integral-equation-based method for accurate analysis of scattering from periodically arranged nanostructures *Phys. Rev.* E **72** 056702

[32] Van Orden D and Lomakin V 2009 Rapidly convergent representations for 2D and 3D Green's functions for a linear periodic array of dipole sources *IEEE Trans. Antennas Propag.* **57** 1973

[33] Beermann J, Novikov S M, Leosson K and Bozhevolnyi S I 2009 Surface enhanced Raman microscopy with metal nanoparticle arrays *J. Opt. A: Pure Appl. Opt.* **11** 075004

[34] Beermann J, Novikov S M, Leosson K and Bozhevolnyi S I 2009 Surface enhanced Raman imaging: periodic arrays and individual metal nanoparticles *Opt. Express* **17** 12698–705

[35] Beermann J, Novikov S M, Albrektsen O, Nielsen M G and Bozhevolnyi S I 2009 Surface-enhanced Raman imaging of fractal shaped periodic metal nanostructures *J. Opt. Soc. Am.* B **26** 2370–6